Garnet coalescence clogs melt extraction channels in migmatite

LITHOS 472–473 (2024) 107581

Contents lists available at ScienceDirect

LITHOS

journal homepage: www.elsevier.com/locate/lithos

Letter

Garnet coalescence clogs melt extraction channels in migmatite

ARTICLE INFO

Keywords
Garnet coalescence
Melt extraction
Lower crustal differentiation
Rheological inversion
Migmatitic metapelites
Serre Massif

ABSTRACT

Here we investigate the evolution of a focused melt extraction horizon exposed in lower crustal metapelites of the Serre Massif in Calabria (southern Variscan belt, Italy) and consider the effect of melt drainage on the rheology of the orogenic lower crust. Our study shows that large (up to >10 cm long) ellipsoidal garnet aggregates associated with a small volume of leucosome in this migmatitic horizon represent clogged melt extraction channels. Using microstructural evidence, particularly electron backscatter diffraction (EBSD) data, we demonstrate that the garnet aggregates formed by coalescence of small peritectic crystals, carried along in anatectic melt migrating towards pull-apart structures, where the melt with entrained garnet pooled as it was progressively squeezed out. Phase equilibrium thermodynamic modelling of melt extraction events indicates that a minimum of 30 vol% of melt was drained out during nearly isobaric heating at average peak pressure (*P*) conditions of 0.97 GPa, from ~700 °C to peak temperatures of 800–840 °C. We use numerical simulations of measured quartz crystallographic preferred orientations (CPOs) to show that melt extraction occurred under pure shear regime. Our results highlight how orogen rheology is conditioned along critical horizons where melting occurs and melt extraction is localized, leaving behind a hard residue.

1. Introduction

Extraction and ascent of anatectic magma from partially molten lower crustal rocks during regional granulite-facies metamorphism have long been studied, since it conditions the evolution of orogens (Brown, 2010; Mehnert, 1968). During anatexis, melt loss occurs as the melt connectivity threshold (MCT) is reached (Rosenberg and Handy, 2005; Vigneresse et al., 1996), connecting mm-sized melt pockets to cm-sized melt channels along shear bands or linked dilatant fractures (Brown, 2007, 2004; Sawyer, 2014; Weinberg and Regenauer-Lieb, 2010). This process, which starts around peritectic minerals where melt initially concentrates (Sawyer, 2014; Vernon and Paterson, 2001; White et al., 2004), is favored by deformation (Bons et al., 2004; Brown et al., 1995; Sawyer et al., 2000) and efficiently allows extraction of large melt volumes in an open system. Conversely, this process is impeded in closed or in low-strain systems, with melt accumulation reaching the rheologically critical melt percentage (RCMP) in rocks (Costa et al., 2009). Mineralogical evidence of anatectic melt loss from residual migmatites and granulites consist of preserved/unretrogressed peritectic minerals in leucosomes (Brown, 2002; White and Powell, 2010, 2002), collapse of formerly melt-filled structures (Brown et al., 1999; Silva et al., 2023), and layers rich in peritectic minerals (Sawyer et al., 2000; White et al., 2004). When these layers develop, peritectic minerals like garnet can grow up to ~15 cm in size and constitute up to 60% of the leucosome, as for the aluminous migmatitic metapelites at Broken Hill (White et al., 2004). However, understanding the formation mechanism of dm-sized garnet in residual migmatites is still challenging.

Here, we present a limiting case of a residual garnet-rich migmatite horizon (Schenk, 1984) from the Serre Massif of Calabria in southern Italy (Fig. 1A), where ellipsoidal garnet exceeds 10 cm in length. These residual migmatites are part of the metapelite unit (Fig. 1A), which records melting between 300 and 270 Ma during the Variscan orogeny (Fornelli et al., 2020, 2011; Micheletti et al., 2008). Despite the remarkable aspect of this horizon and the potential implication for orogen evolution (Tursi et al., 2020), it has not yet been studied in detail. We document focused anatectic melt extraction during pure shear dominated-deformation from this horizon in the Amaroni–Vallefiorita area (Fig. 1A), where such long ellipsoidal garnets are spectacularly exposed (Fig. 1B–D), and achieve their size and shape through coalescence of small peritectic garnets.

2. Material and methods

We carried out detailed geological mapping at 1:5000 scale, together with meso- to micro-structural studies in the Amaroni–Vallefiorita area (Fig. 1A). Oriented samples (Table S1) were collected throughout the residual coarse-grained garnet migmatite horizon (Fig. 1A). Microstructural analysis combined with EBSD mapping tie the growth mechanism of the large ellipsoidal garnets with the prevailing deformation regime. We simulate measured quartz pole figures using D-Rex software (Kaminski et al., 2004) to constrain the kinematic vorticity and the amount of shortening. Mineral composition and X-ray elemental maps were obtained through energy-dispersive X-ray spectroscopy (EDS) on polished, carbon coated thin sections. The reaction forming the peritectic minerals was balanced through the least-squares method (Fisher, 1989), using PCalc freeware software (Godard, 2010). The *P–T* conditions of equilibration and the volume of melt extracted were derived through forward thermodynamic modelling of amphibolite-facies metapelites exposed in the southern Serre Massif. Sample MAM_2 from Acquafredda et al. (2003) was used as representative for the bulk-rock composition of the residual coarse-grained garnet migmatites before melting. Details on methodology and modelling strategies are reported

https://doi.org/10.1016/j.lithos.2024.107581
Received 4 September 2023; Received in revised form 5 March 2024; Accepted 12 March 2024
Available online 19 March 2024

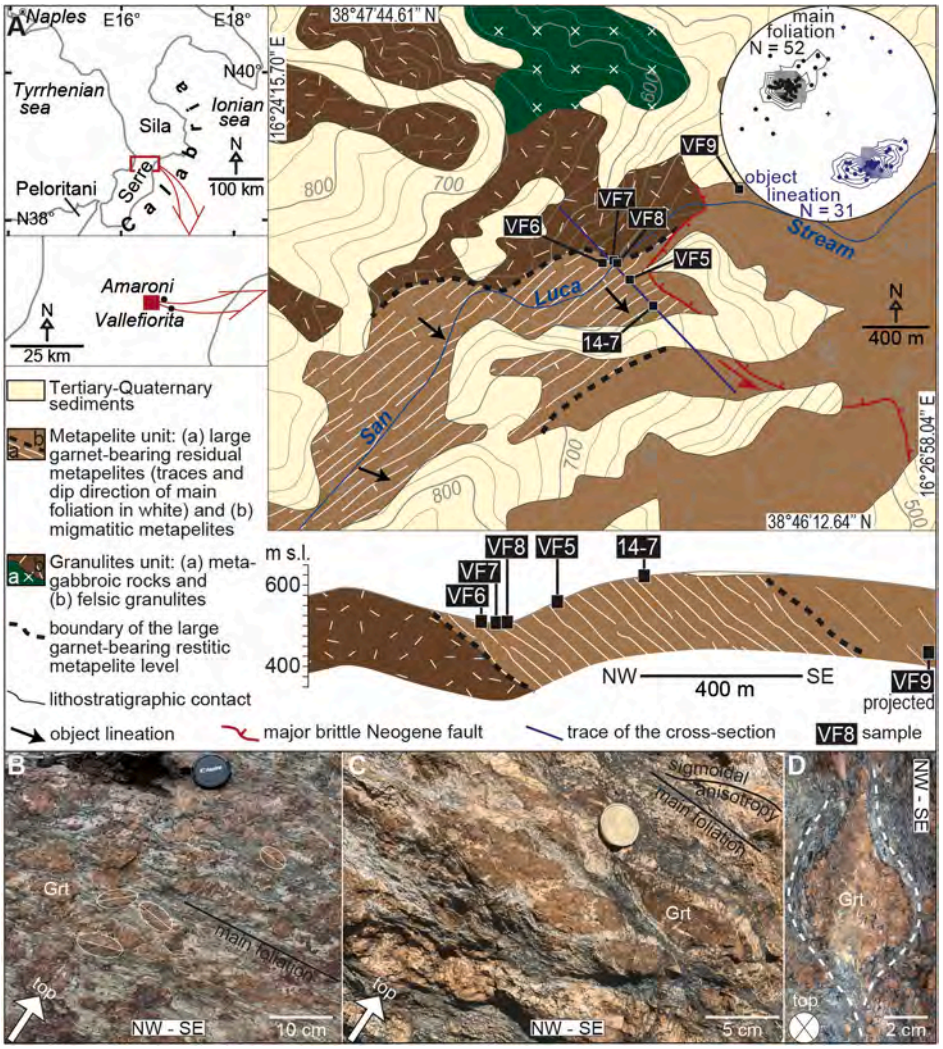

Fig. 1. (A) Geological sketch map of the study area and geologic profile across the residual coarse-grained garnet migmatite level; the location of the studied samples and the stereographic projection of poles to foliation and lineation in the residual migmatite level are included (equal area lower hemisphere, 1% area contour, C.I. = 4%/1% area; data processed with Stereonet OSX by Cardozo and Almendinger, 2013). (B) Typical residual coarse-grained garnet migmatite cropping out in the study area; the representative white ellipses simulating the shape of the large garnets show opposite dip of the long axis with respect to the main foliation, indicating contrasting kinematics. (C) Melanocratic and leucocratic layers defining the main foliation; sigmoidal-shaped planar anisotropies are also shown. (D) Grain lineation on the main foliation; note Sil enveloping the large, elongated Grt, as indicated by the dashed lines.

in the Supplementary Material together with CPO data, mineral compositions and balancing of the reaction (Tables S2–S3). Mineral abbreviations follow Whitney and Evans (2010).

3. Results

3.1. The residual coarse-grained garnet migmatite level

In the San Luca stream valley, the contact between the granulite unit, below, and the metapelite unit, above, is marked by a 600 m-thick and >3 km-long, SE-dipping horizon of residual migmatites (Fig. 1A). This residual horizon, containing ellipsoidal garnets up to 10 cm in size, formed at the expense of partially molten metapelites depleted of their melt (Fig. 1). Across this level, the large garnets are typically accompanied by small volumes of connected and disconnected leucosome, and wrapped by mm- to cm-thick biotite-sillimanite melanosome layers tracing the main foliation (Fig. 1B–D). This generally strikes NE-SW and dips ~40° towards SE (Fig. 1A), closely parallel to the contact between the two granulite-facies units (Fig. 1A). The lineation consists of preferentially aligned (i) quartz-feldspar stretched aggregates, (ii) large ellipsoidal garnets, and (iii) mm-long sillimanite prisms which geometrically adapt to the garnet shape (Fig. 1D), plunging 30–40° towards SE (Fig. 1A). The arrangement of the long axis of the ellipsoidal garnets with respect to the main foliation (e.g., Fig. 1C), together with the object lineation trend (Fig. 1A), indicates contrasting top-to-the-NW or top-to-the-SE kinematics, in the present geographic coordinates.

3.2. Leucosome formation, evidence of partial melting and types of garnet and K-feldspar

The biotite-sillimanite foliation in the melanosome (Fig. 2A–C) envelops millimetric ellipsoidal pockets of leucosome consisting of quartz, garnet and K-feldspar, with small biotite and sillimanite inclusions within garnet and quartz, the latter showing low dihedral angles along grain boundaries (Fig. 2C). In these sites garnet is sub-millimetric and has nearly constant Alm composition, with X_{Fe} increasing from ~0.71–0.72 in the core to ~0.75–0.76 towards the rim, with Grs <4 mol % and Sps <2 mol% (Table S2). Biotite shows no compositional variation from core to rim (Table S2), with the different grains varying in X_{Fe} from ~0.35 to ~0.43 (Table S2). When garnet becomes millimetric in size, biotite, sillimanite/fibrolite, quartz, rutile, and K-feldspar can be included, forming an internal foliation continuing with the external that

symmetrically envelops garnet (Fig. 2A–B). Accordingly, garnet, K-feldspar and melt formed together by the reaction:

$$Bt + Sil + Ilm + Qz = Grt + Kfs + Rt + Liq. \quad (R1)$$

Reaction R1 can be balanced adding Ca to reactants and Na to products through the $Ca_{-1.00}Na_{+1.00}$ substitution vector (Table S3), indicating absence of a reactant mineral (Adjerid et al., 2015, 2013; Godard, 2010). The substitution vector takes into account involvement of plagioclase in R1, which likely carried Ca for the grossular fraction into garnet. Evidently, plagioclase was completely consumed since it was not observed in our samples, consistent with the phase equilibrium thermodynamic modelling discussed later. Garnet reaches its maximum size (Figs. 1, S1) in the leucosome bands and pockets. The leucosome consists of K-feldspar, quartz and garnet, with few sillimanite and biotite. K-feldspar can be divided into three microstructural types (Fig. 2D–G): (i) anhedral to subhedral crystals with minor inclusions of quartz and sillimanite/fibrolite, (ii) anhedral poikilitic grains including oriented trails of sillimanite, quartz and biotite, and (iii) intergranular K-feldspar including small euhedral to subhedral garnet. These represent crystallized K-feldspar from melt (Type-I), peritectic K-feldspar (Type-II), and pseudomorphs after interstitial melt (Type-III) (sensu Dyck et al., 2020; Ganzhorn et al., 2016; Holness and Sawyer, 2008), respectively. The margin of the developing large garnet porhyroblasts is typically poikilitic (Figs. 2H, S2); small garnets with rounded to lobate boundaries are intergrown with elongated, polygranular quartz, ilmenite/rutile, biotite and some K-feldspar and sillimanite (Figs. 2H, S2). These small garnet grains coalesce with each other (Figs. 2I–J, S2) and sometimes show facets at the contact (Fig. 2H). Euhedral garnet is mostly found when included in Type-I and Type-III K-feldspar, and forms low dihedral angles when in contact with quartz (Fig. 2G). In general, nucleation in the SiO_2-rich domains or in the Al_2O_3-rich domains, allows us to differentiate garnet in two types: small Type-S and larger Type-A grains (Fig. 2), respectively. This discrimination follows Lobjoie et al. (2020), who observed a similar bimodal distribution of garnet in the Khondalite Belt of the North China craton.

3.3. Microstructure of coalesced large ellipsoidal garnet

Five thin sections have been cut from the large ellipsoidal garnet aggregate shown in Fig. S1, all parallel to the X-Z plane of the strain ellipsoid; The EBSD and mineral analyses discussed have been performed on two of them (VF6–2; VF6–5). Thin section VF6–2 (Fig. 3), shows that different portions of the large ellipsoidal garnet preserve distinct microstructures: the uniformly blue-coloured central portion (IPF colour coded EBSD map, Fig. 3A) is characterized by lobate and cuspate garnet-K-feldspar interphase boundaries due to the pronounced embayment of K-feldspar. There, Type-I K-feldspar is associated with quartz, biotite, ilmenite, rutile and sillimanite. Besides the large interconnected Type-I K-feldspar embayment, smaller isolated K-feldspar and biotite inclusions characterise this central garnet portion. Towards the lower part (Fig. 3A, yellow-contoured area), a 2 mm-thick embayment of Type-II K-feldspar occurs. The blue-coloured central garnet portion is flanked on its left by quartz- or garnet-rich layers about 1 cm-thick. Here, small anhedral to subhedral garnets with distinct crystallographic orientation, occur (Fig. 3). They form trains or isolated aggregates, and coalesce at the contact with the large blue-coloured central garnet. The shape of the single garnet crystals is mainly constrained by the quartz (and subordinately by K-feldspar and ilmenite) interface boundaries, whose lobate forms indicate quartz dissolution when it was in contact with melt (Ganzhorn et al., 2016). Inside the small garnets, inclusions of quartz, biotite, ilmenite and rutile are preserved. Therefore, the blue-coloured central portion is a Type-A garnet, while that in the quartz-rich band is of Type-S. Hence, Type-S garnet and Type-II K-feldspar grew within μm- to mm-thick melt channels (e.g., Fig. 2G), wherein fine-grained reactants (e.g., biotite and sillimanite) were transported, as observed experimentally by Ganzhorn et al. (2016). The Kernel Average Misorientation (KAM) map in Fig. 3B shows crystallographic mismatch reduction once the small Type-S garnets come into contact with the large Type-A garnet, although mismatches larger than 10° are still visible in the central left part. Albeit crystallographic mismatches still exist among coalesced grains (Fig. 3E), the elemental maps (Fig. 3H–K) and the traverse of analysis points (Fig. S4) do not show any appreciable compositional variation in major elements along low misorientation boundaries. Microstructures and EBSD data suggest that migration and rotation of small Type-S garnets was driven by dissolution of quartz along melt films. Once coalescence of several small garnet grains with the central large Type-A garnet occurred (Fig. 3B), the melt flow along dissolved quartz bands was obstructed. Evidence for melt channels clogged by small peritectic garnet and rutile, together with K-feldspar and quartz crystallized from the melt, is observed in the upper right of the bluish-coloured garnet (Fig. 3A, yellow square). Subtle crystallographic orientation differences occur between the small garnet grains separated from the surrounding large garnet by K-feldspar and by the thin boudinaged tear drop-like quartz film at the right (Fig. 3C, F). Maximum mismatch between garnet inside the melt channel and outside is 8° (green-coloured garnet contacts in Fig. 3C, clusters of poles in Fig. 3F).

Along the rim portion (Fig. 3A, D), aligned subgrain boundaries separate the spur of the ellipsoidal garnet from the inner part. Small aligned subgrains are also observed along what might have been the contact zone between coalesced garnets (Fig. 3E). These microstructures support plastic deformation to have occurred along localized external parts of Type-A garnets along glide/slip systems disposed orthogonally to each other. This subgrain geometry is significantly different from that between Type-S and Type-A coalescing garnet (Fig. 3B).

3.4. Measured and simulated CPOs

In thin section VF6–5, a 1- to 2-cm thick and 4-cm long quartz layer within the periphery of the coalesced, ellipsoidal garnet (Fig. S1) has been analysed. The 300–800 μm-large quartz grains show dynamic recrystallisation and grain boundary migration (Fig. S3A). In addition, we have measured quartz grains within a 2.5 cm-long and 1 cm-thick recumbent fold in sample 6VF8 (Fig. S3B). For the construction of the pole figures, one indexed point per grain was considered to avoid any bias by the grain size, resulting in a dataset of 253 and 270 points, respectively. Simulation through D-Rex was used to constrain the deformation parameters during melt extraction. The fundamental characteristics of the simulated pole figures are strikingly similar to the measured one (Figs. 4A, S3). The key parameters of the simulations (Table S4) indicate that: (i) the pole figures are successfully reproduced only if the kinematic vorticity (W_k) is set to 0, implying that deformation inducing melt extraction was pure shear; (ii) vertical shortening is on the order of ~50%; (iii) the deformation mechanism was dislocation creep, and the slip systems involved were prism [c] slip assisted by minor basal <a> slip. The dispersed small secondary c-axis maxima suggest that some additional deformation mechanism may have assisted dislocation creep and caused pole density differences between measured and simulated data.

3.5. Melt extraction during garnet coalescence

To infer the amount of melt expelled from the residual migmatite horizon during garnet coalescence, modelling of melt extraction events in open systems follows Yakymchuk and Brown (2014). The mineral relationships observed (Figs. 2, 3) indicate that Grt-Sil-Kfs-Bt-Qz-Rt-Ilm comprise the peak mineral assemblage, and that, in general, the rock records complete equilibration at peak metamorphic conditions. This is corroborated by (i) the almost flat garnet zoning profiles showing no resorption at the rim (Fig. S4) and, (ii) the lack of retrogression of peritectic minerals (Fig. 2) indicating that no melt-residue interaction occurred after the metamorphic peak. A first *P–T* pseudosection for high-

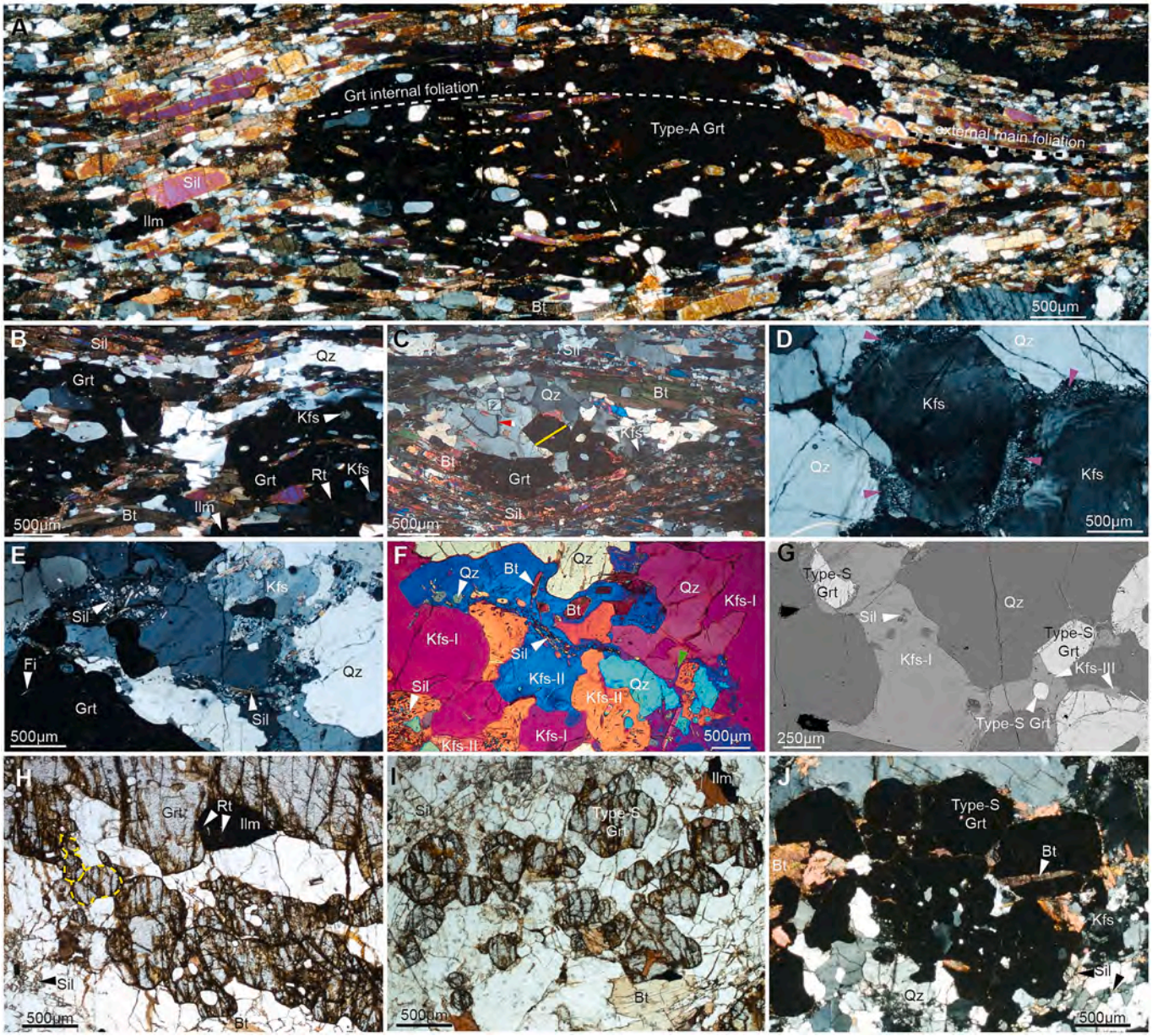

Fig. 2. (A) Micrograph collage showing mm-sized ellipsoidal Type-A Grt with the long axis sub-parallel to the stretching lineation; note the continuity between the garnet internal foliation defined by quartz, K-feldspar, sillimanite and biotite inclusions and the external main foliation deflecting around garnet; cross-polarized light (CPL). (B) Adjacent mm-sized poikilitic garnets separated by quartz grains; note the quartz aggregates hosting biotite and sillimanite, included in garnets; CPL. (C) A reacting microdomain where garnet grows into an ellipsoidal pocket of leucosome; note the small sillimanite and biotite included into quartz and the melt pseudomorphs (red arrow); CPL. The yellow bar delineates the traverse of point analysis in Fig. S4A. (D) Inclusion-free, subhedral K-feldspar decorated by micrographic intergrowths (magenta arrows) along the quartz–K-feldspar grain boundary; CPL. (E) Intergranular anhedral K-feldspar between quartz and garnet, including trails of fine-grained sillimanite; note fibrolite inclusions into garnet; CPL. (F) Anhedral K-feldspar poikiloblasts and porphyroblasts, representing Type-I and Type-II Kfs discussed in the text; the green arrow indicates K-feldspar pseudomorphing melt (Type-III Kfs); CPL with λ/2 Qz plate. (G) Inclusion-poor Type-I Kfs and Type-III Kfs including subhedral to euhedral Type-S Grt grains; SEM-BSE image. (H) Margin of cm-sized poikilitic garnet where sub-millimetric sized subhedral to euhedral grains can be still observed (dashed yellow-contoured grain-boundaries); plane-polarized light (PPL). (I) Cluster of subhedral to euhedral, sub-millimetre grains of Type-S Grt; PPL. (J) Millimetric aggregate of subhedral to euhedral grains of Type-S Grt; note intergranular sites between coalescing garnets mostly occupied by biotite and quartz; in some sites garnet grows along biotite cleavage planes; CPL. (For interpretation of the references to colour in this figure legend, the reader is referred to the web version of this article.)

P (~1.5 GPa) saturated wet-solidus was calculated, considering the LOI amount for H_2O (Figs. 4B, S5). The equilibrium mineral assemblage is stable in the range of ~0.91–1.03 GPa and ~ 790–830 °C, bracketed at high-*P* by the Ky to Sil transition, at low-*P* by the Rt-out curve and at high-*T* by the Bt-out curve (Figs. 4B, S5). As melt drained from the melt-bearing horizon, the density of the residue increased, hampering exhumation. Consequently, the evolution under drained conditions from the wet-solidus to the metamorphic peak can be modelled through an isobaric-heating path at the average *P* of 0.97 GPa (Fig. 4B). The 6 vol% of melt was extracted each time the MCT was reached, resulting into progressively more residual compositions (Table S5), shifting the solidus towards higher-*T* (Fig. S5); in the specific case, after five melt extraction events the peak mineral assemblage is in equilibrium with <4 vol% of melt at ~800–840 °C (Fig. 4B). Accordingly, ~30 vol% of melt has been extracted from the coarse-grained garnet residual migmatite level during granulite-facies metamorphism.

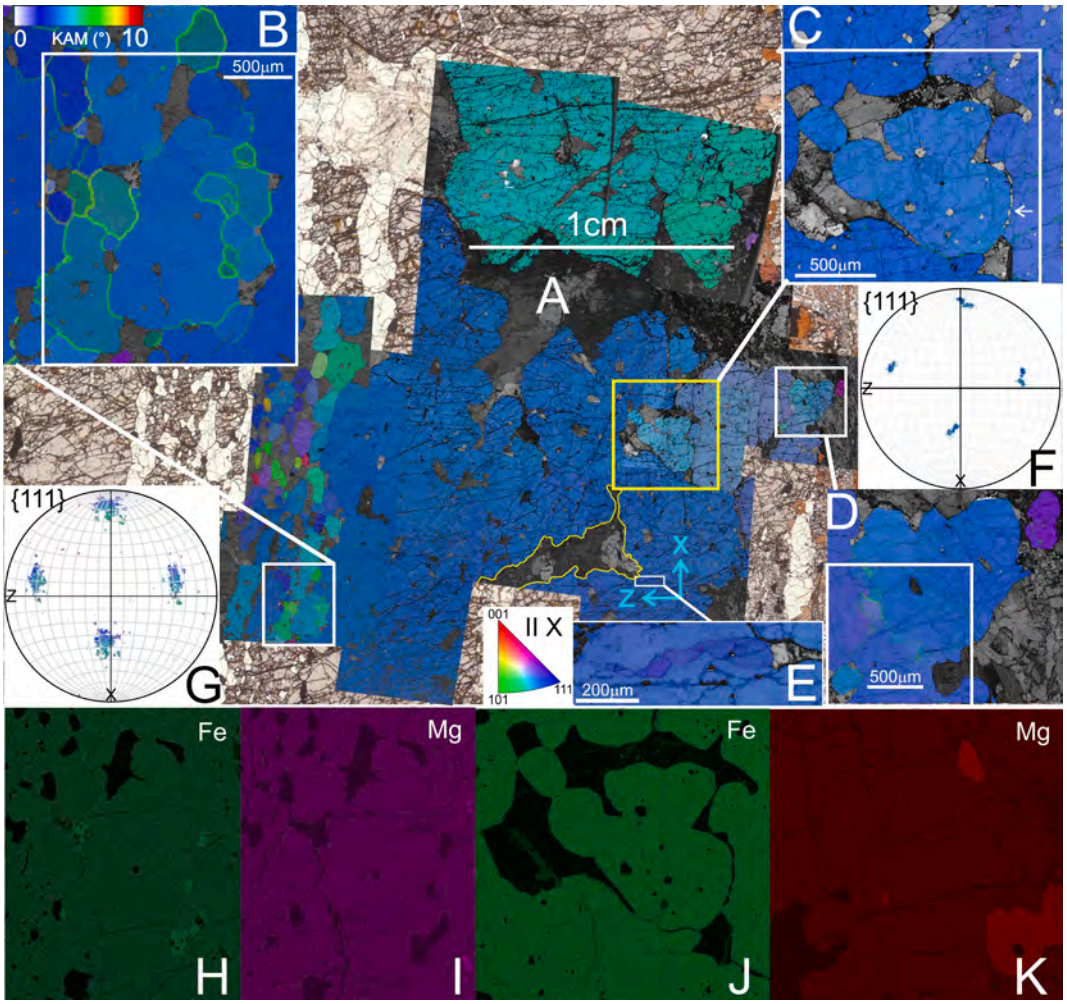

Fig. 3. (A) Montage of 18 EBSD maps overlain on scanned thin section VF6-2. Type-A Grt (central blue IPF colour-coded portion) shows no grain boundaries. Large Type-I Kfs embayment (medium grey) form lobate to cuspate interface boundaries with Type-A Grt as well as Type-II Kfs (yellow contoured). Note the trains of small elongated Type-S Grt intergrown with quartz, coalescing with each other and with Type-A Grt. (B) KAM map (blow-up) showing coalesced Type-S Grt with still visible misorientation of (sub)grain boundaries (see also pole figure in Fig. 3G); the white rectangle refers to Fe and Mg maps (H and I respectively). (C) Melt channel clogged by crystallisation of garnet and K-feldspar; the KAM map is a blow-up with internal garnets light-blue coloured (IPF colour coding). Misorientations at contact zones with surrounding garnet is ~8° (see also pole figure in Fig. 3F); note the tear drop-like quartz film (white arrow) formed during garnet rotation. (D) Aligned subgrain boundaries along the outer spur of Type-A garnet. (E) Aligned subgrains along the contact zone of former single garnet grains. (F–G) Pole figures of garnet misorientation (sub)grain boundaries; lower hemisphere equal area projections. (H–K) Fe and Mg X-ray maps acquired within the white rectangles shown in (B), (C) and (D); no compositional zoning can be appreciated; areas with different intensities are inclusions. (For interpretation of the references to colour in this figure legend, the reader is referred to the web version of this article.)

4. Discussion and conclusion

Ellipsoidal garnet aggregates up to 10 cm in length associated with a limited volume of leucosome have been described before (e.g., White et al., 2004), but the mechanism by which they form has not been characterized in detail and can be understood based on this study in the Amaroni–Vallefiorita area (Fig. 4Ct1–t2). The key aspect is not diffusion-controlled growth of garnet around a single nucleus (White et al., 2004), but small peritectic garnet carried with the melt into progressively opening pulled apart pools (Fig. 4Ct1a–c). Opening of pull-apart-type structures, is controlled by staircase trajectories of conjugate enveloping foliations (Fig. 4Ct1, t1a–c). The dynamic evolution of the pools during pure shear deformation induces local depressurization during opening (attracting fluid/melt, e.g. stepped veins and lozenge-shaped structures as in Bons et al., 2012) with garnet-rich melt sucked in and peritectic minerals-depleted melt squeezed out, leaving coalesced garnet grains behind (Fig. 4C, t1a-e). In this dynamic system coalescence of garnet in melt pools and progressive melt extraction below the MCT occurred during a total of ~50% vertical shortening (Fig. 4Ct1-t2). This is testified by microstructures (Figs. 2, 3) and physical parameters as strain and kinematic vorticity (Table S4) derived from simulated quartz CPOs (Fig. 4A, in line with Festa et al., 2012). Garnet coalescence and growth under subsolidus conditions has already been shown by Spiess et al. (2001), where grain rotation was accommodated by diffusive mass transfer processes (Herrmann et al., 1976), grain boundary dislocations glide (Sutton and Balluffi, 1987) or dissolution-precipitation creep (Bons and Den Brok, 2000). Garnet rotation towards a common crystallographic orientation along melt-rich interfaces is much more efficient, and reasonably accounts for coalescence of Type-A garnets (Fig. 3A). Here grain boundaries are no longer recognized, similarly as for the small amalgamated garnets in Taylor and Stevens (2010). On the other hand, our EBSD maps (Fig. 3) support coalescence of small Type-S garnet with the large Type-A garnet (Fig. 3B, G). The small garnets pooled whereas interleaved quartz layers were dissolved in the presence of melt. Crystallographic mismatch reduction (Fig. 3B, C, E, G) requires garnet rotation. This is best exemplified along the right-hand boundary of the melt channel (Fig. 3C), where tear-drop shaped quartz microstructures occur between coalescing grains (Fig. 3F). Eventually, garnet

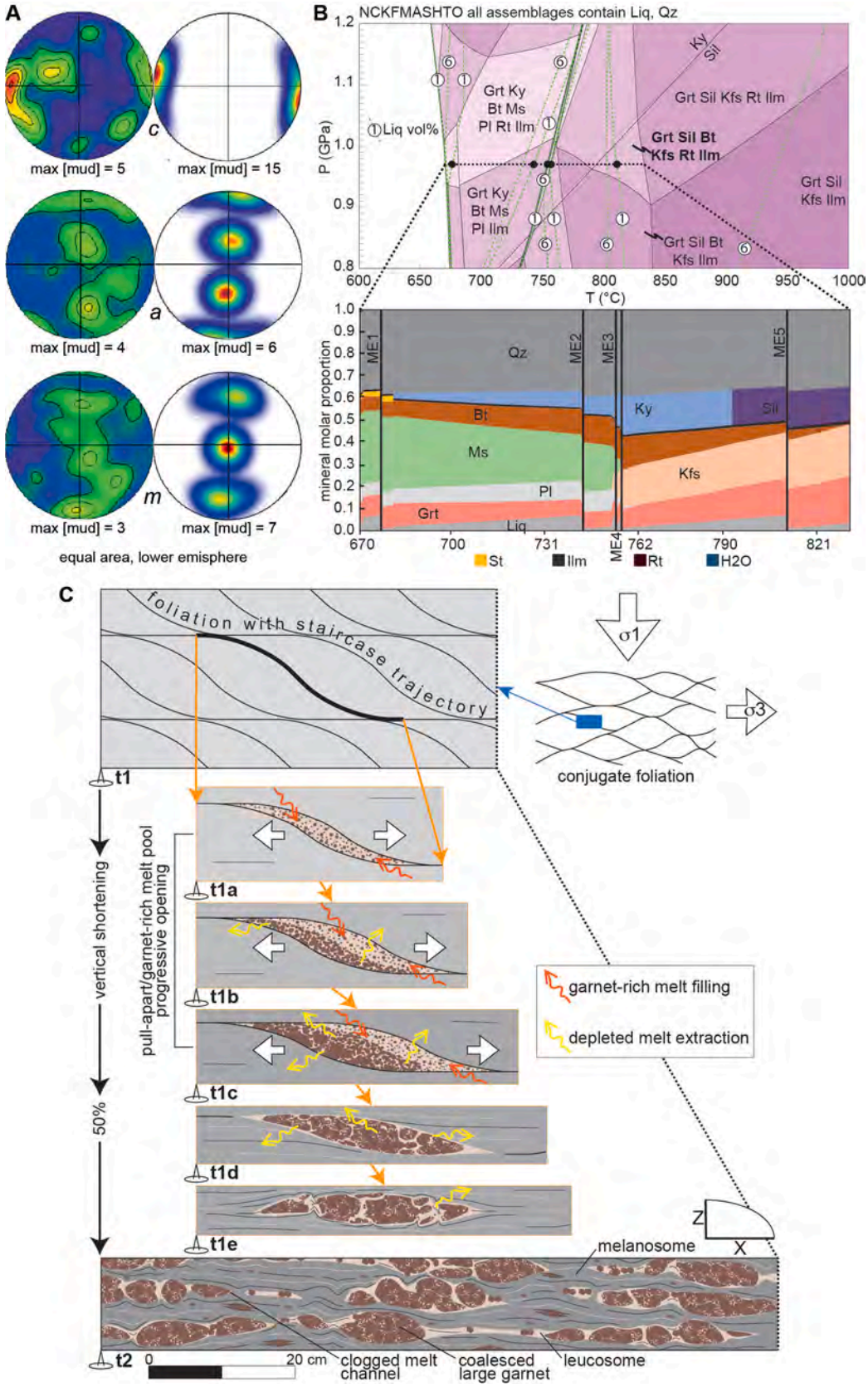

Fig. 4. (A) Measured (left) and modelled (right) quartz CPOs (details in supplementary material). (B) Cumulative suprasolidus *P–T* phase diagram (top) for sample MAM_2 comprising six pseudosections arranged from low- to high-*T* after five melt extraction events (ME) (black dots). The black dashed line delineates the path to the peak mineral assemblage (bold); variation of minerals molar proportion along the path (bottom) is also shown. (C) Modelled formation of coarse-grained garnet from frame t1 to t2. In the top right inset of t1, conjugate symmetrically arranged foliations under vertical shortening are redrawn after Fossen and Cavalcante

(2017); one set of conjugate foliations, with staircase trajectories, is shown for simplification in t1. In the frames t1a–e the formation of coarse-grained garnet in a single pull-apart, is highlighted.

coalescence clogs melt channels. Fig. 3D–E shows aligned subgrains along potential contacts between coalesced former single garnet grains. These aligned subgrain bounderies suggest that as melting ceased at peak metamorphic conditions, because of biotite consumption (Fig. 4B), large ellipsoidal garnets formed the stress sustaining framework (Fig. 4Ct2). This resulted locally in plastic deformation of garnet, likely along former boundaries between coalesced grains. Overall, the whole process from partial melting to melt extraction resulted in crustal differentiation forming a garnet-rich horizon and in a significant rheological inversion as loss of ~30 vol% of melt provoked hardening of the lower crust.

Supplementary data to this article can be found online at https://doi.org/10.1016/j.lithos.2024.107581.

Declaration of competing interest

The authors declare that they have no known competing financial interests or personal relationships that could have appeared to influence the work reported in this paper.

Acknowledgments

RS thanks Manuele Faccenda for introducing him to D-Rex. This research was financially supported by “Fondo per le Attività Base di Ricerca–2017” to VF, DOR2018 by University of Padua and Italian PRIN 20178LPCP to RS, and “Ricerca Locale 2023” by University of Turin to FT. We are grateful to Michael Brown, Thomas Chacko and an anonymous reviewer for their constructive criticism and suggestions which have improved substantially the original manuscript. Nadia Malaspina is thanked for her careful editorial handling.

References

Acquafredda, P., FornelliI, A., Micheletti, F., Piccarreta, G., 2003. The abundance of 51 elements and petrovolumetric models of the Calabria crust: Curinga-Stilo area (site 6). In: Sassi, F.P., Cesare, B., Mazzoli, C., Peruzzo, L., Rizzo, G., Sassi, R., Spiess, R. (Eds.), The Abundance of 55 Elements and Petrovolumetric Models of the Crust in 9 Type Areas from the Crystalline Basements of Italy, with some Geophysical and Petrophysical Data. Accademia Nazionale Delle Scienze Detta Dei Xl, Roma, pp. 263–288.

Adjerid, Z., Godard, G., Ouzegane, K., Kienast, J.R., 2013. Multistage progressive evolution of rare osumilite-bearing assemblages preserved in ultrahigh-temperature granulites from in Ouzzal (Hoggar, Algeria). J. Metamorph. Geol. 31, 505–524. https://doi.org/10.1111/jmg.12031.

Adjerid, Z., Godard, G., Ouzegane, K., 2015. High-pressure whiteschists from the Ti-N-Eggoleh area (Central Hoggar, Algeria): a record of Pan-African oceanic subduction. Lithos 226, 201–216. https://doi.org/10.1016/j.lithos.2015.02.013.

Bons, P.D., Den Brok, B., 2000. Crystallographic preferred orientation development by dissolution-precipitation creep. J. Struct. Geol. 22, 1713–1722. https://doi.org/10.1016/S0191-8141(00)00075-4.

Bons, P.D., Arnold, J., Elburg, M.A., Kalda, J., Soesoo, A., van Milligen, B.P., 2004. Melt extraction and accumulation from partially molten rocks. Lithos 78, 25–42. https://doi.org/10.1016/j.lithos.2004.04.041.

Bons, P.D., Elburg, M.A., Gomez-Rivas, E., 2012. A review of the formation of tectonic veins and their microstructures. J. Struct. Geol. 43, 33–62. https://doi.org/10.1016/j.jsg.2012.07.005.

Brown, M., 2002. Retrograde processes in migmatites and granulites revisited. J. Metamorph. Geol. 20, 25–40. https://doi.org/10.1046/j.0263-4929.2001.00362.x.

Brown, M., 2004. The mechanism of melt extraction from lower continental crust of orogens. Spec. Pap. Geol. Soc. Am. 389, 35–48. https://doi.org/10.1130/0-8137-2389-2.35.

Brown, M., 2007. Crustal melting and melt extraction, ascent and emplacement in orogens: mechanisms and consequences. J. Geol. Soc. Lond. 164, 709–730. https://doi.org/10.1144/0016-76492006-171.

Brown, M., 2010. Melting of the continental crust during orogenesis: the thermal, rheological, and compositional consequences of melt transport from lower to upper continental crust. Can. J. Earth Sci. 47, 655–694. https://doi.org/10.1139/E09-057.

Brown, M., Averkin, Y.A., McLellan, E.L., Sawyer, E.W., 1995. Melt segregation in migmatites. J. Geophys. Res. 100 https://doi.org/10.1029/95jb00517.

Brown, M.A., Brown, M., Carlson, W.D., Denison, C., 1999. Topology of syntectonic melt-flow networks in the deep crust: Inferences from three- dimensional images of leucosome geometry in migmatites. Am. Mineral. 84, 1793–1818.

Cardozo, N., Almendinger, R.W., 2013. Spherical projections with OSXStereonet. Comput. Geosci. 51, 193–205.

Costa, A., Caricchi, L., Bagdassarov, N., 2009. A model for the rheology of particle-bearing suspensions and partially molten rocks. Geochem. Geophys. Geosyst. 10, 1–13. https://doi.org/10.1029/2008GC002138.

Dyck, B., Waters, D.J., St-Onge, M.R., Searle, M.P., 2020. Muscovite dehydration melting: reaction mechanisms, microstructures, and implications for anatexis. J. Metamorph. Geol. 38, 29–52. https://doi.org/10.1111/jmg.12511.

Festa, V., Fornelli, A., Paglionico, A., Pascazio, A., Piccarreta, G., Spiess, R., 2012. Asynchronous extension of the late-Hercynian crust in Calabria. Tectonophysics 518–521, 29–43. https://doi.org/10.1016/j.tecto.2011.11.007.

Fisher, G.W., 1989. Matrix analysis of metamorphic mineral assemblages and reactions. Contrib. Mineral. Petrol. 102 https://doi.org/10.1007/BF01160191.

Fornelli, A., Pascazio, A., Piccarreta, G., 2011. Diachronic and different metamorphic evolution in the fossil Variscan lower crust of Calabria. Int. J. Earth Sci. 101, 1191–1207. https://doi.org/10.1007/s00531-011-0721-8.

Fornelli, A., Festa, V., Micheletti, F., Spiess, R., Tursi, F., 2020. Building an orogen: review of U-Pb zircon ages from the Calabria-Peloritani terrane to constrain the timing of the southern variscan belt. Minerals 10, 1–29. https://doi.org/10.3390/min10110944.

Fossen, H., Cavalcante, G.C.G., 2017. Shear zones – a review. Earth Sci. Rev. 171, 434–455. https://doi.org/10.1016/j.earscirev.2017.05.002.

Ganzhorn, A.C., Trap, P., Arbaret, L., Champallier, R., Fauconnier, J., Labrousse, L., Prouteau, G., 2016. Impact of gneissic layering and localized incipient melting upon melt flow during experimental deformation of migmatites. J. Struct. Geol. 85, 68–84. https://doi.org/10.1016/j.jsg.2016.02.004.

Godard, G., 2010. Two orogenic cycles recorded in eclogite-facies gneiss from the southern Armorican Massif (France). Eur. J. Mineral. 21, 1173–1190. https://doi.org/10.1127/0935-1221/2009/0021-1984.

Herrmann, G., Gleiter, H., Baro, G., 1976. Investigation of low energy grain boundaries in metals by a sintering technique. Acta Metall. 24, 353–359.

Holness, M.B., Sawyer, E.W., 2008. On the pseudomorphing of melt-filled pores during the crystallization of migmatites. J. Petrol. 49, 1343–1363. https://doi.org/10.1093/petrology/egn028.

Kaminski, É., Ribe, N.M., Browaeys, J.T., 2004. D-Rex, a program for calculation of seismic anisotropy due to crystal lattice prefferred orientation in the convective upper mantle. Geophys. J. Int. 158, 744–752. https://doi.org/10.1111/j.1365-246X.2004.02308.x.

Lobjoie, C., Trap, P., Oliot, E., Lin, W., Barou, F., Goncalves, P., Marquer, D., 2020. Rheological behavior of high temperature garnet-bearing migmatites: the Khondalite Belt example (North China Craton). J. Struct. Geol. 131, 103910 https://doi.org/10.1016/j.jsg.2019.103910.

Mehnert, K.R., 1968. Migmatites and the Origin of Granitic Rock. Elsevier Sciences, New York.

Micheletti, F., Fornelli, A., Piccarreta, G., Barbey, P., Tiepolo, M., 2008. The basement of Calabria (southern Italy) within the context of the Southern European Variscides: LA-ICPMS and SIMS U-Pb zircon study. Lithos 104, 1–11. https://doi.org/10.1016/j.lithos.2007.11.003.

Rosenberg, C.L., Handy, M.R., 2005. Experimental deformation of partially melted granite revisited: Implications for the continental crust. J. Metamorph. Geol. 23, 19–28. https://doi.org/10.1111/j.1525-1314.2005.00555.x.

Sawyer, E.W., 2014. The inception and growth of leucosomes: Microstructure at the start of melt segregation in migmatites. J. Metamorph. Geol. 32, 695–712. https://doi.org/10.1111/jmg.12088.

Sawyer, E.W., Dombrowski, C., Collins, W.J., 2000. Movement of melt during synchronous regional deformation and granulite-facies anatexis, an example from the Wuluma Hills, Central Australia. Geol. Soc. Spec. Publ. 168, 221–237. https://doi.org/10.1144/GSL.SP.1999.168.01.15.

Schenk, V., 1984. Petrology of felsic granulites, metapelites, metabasics, ultramafics, and metacarbonates from Southern Calabria (Italy): prograde metamorphism, uplift and cooling of a former lower crust. J. Petrol. 25, 255–296. https://doi.org/10.1093/petrology/25.1.255.

Silva, D., Piazolo, S., Daczko, N.R., 2023. Trapped K-feldspar phenocrysts as a signature of melt migration pathways within active high-strain zones. J. Metamorph. Geol. 41, 351–375. https://doi.org/10.1111/jmg.12698.

Spiess, R., Peruzzo, L., Prior, D.J., Wheeler, J., 2001. Development of garnet porphyroblasts by multiple nucleation, coalescence and boundary driven rotations. J. Metamorph. Geol. 19, 269–290. https://doi.org/10.1046/j.0263-4929.2000.00311.x.

Sutton, A., Balluffi, R., 1987. On geometric criteria for low interfacial energy. Acta Metall. 35, 2177–2201.

Taylor, J., Stevens, G., 2010. Selective entrainment of peritectic garnet into S-type granitic magmas: evidence from Archaean mid-crustal anatectites. Lithos 120, 277–292. https://doi.org/10.1016/j.lithos.2010.08.015.

Tursi, F., Spiess, R., Festa, V., Fregola, R.A., 2020. Hercynian subduction-related processes within the metamorphic continental crust in Calabria (southern Italy). J. Metamorph. Geol. 38, 771–793. https://doi.org/10.1111/jmg.12537.

Vernon, R.H., Paterson, S.R., 2001. Axial-surface leucosomes in anatectic migmatites. Tectonophysics 335, 183–192. https://doi.org/10.1016/S0040-1951(01)00049-X.

Vigneresse, J.L., Barbey, P., Cuney, M., 1996. Rheological transitions during partial melting and crystallization with application to felsic magma segregation and transfer. J. Petrol. 37, 1579–1600. https://doi.org/10.1093/petrology/37.6.1579.
Weinberg, R.F., Regenauer-Lieb, K., 2010. Ductile fractures and magma migration from source. Geology 38, 363–366. https://doi.org/10.1130/G30482.1.
White, R.W., Powell, R., 2002. Melt loss and the preservation of granulite facies mineral assemblages. J. Metamorph. Geol. 20, 621–632. https://doi.org/10.1046/j.1525-1314.2002.00206.x.
White, R.W., Powell, R., 2010. Retrograde melt-residue interaction and the formation of near-anhydrous leucosomes in migmatites. J. Metamorph. Geol. 28, 579–597. https://doi.org/10.1111/j.1525-1314.2010.00881.x.
White, R.W., Powell, R., Halpin, J.A., 2004. Spatially-focussed melt formation in aluminous metapelites from Broken Hill, Australia. J. Metamorph. Geol. 22, 825–845. https://doi.org/10.1111/j.1525-1314.2004.00553.x.
Whitney, D.L., Evans, B.W., 2010. Abbreviations for names of rock-forming minerals. Am. Mineral. 95, 185–187. https://doi.org/10.2138/am.2010.3371.
Yakymchuk, C., Brown, M., 2014. Consequences of open-system melting in tectonics. J. Geol. Soc. Lond. 171, 21–40. https://doi.org/10.1144/jgs2013-039.

Vincenzo Festa[a], Richard Spiess[b], Fabrizio Tursi[c,*]
[a] *Department of Earth and Geo-Environmental Sciences, University of Bari Aldo Moro, via E. Orabona, 4, 70125 Bari, Italy*
[b] *Department of Geosciences, University of Padua, via G. Gradenigo, 6, 35131 Padova, Italy*
[c] *Department of Earth Sciences, University of Turin, via V. Caluso, 35, Turin 10125, Italy*

[*] Corresponding author.
E-mail address: fabrizio.tursi@unito.it (F. Tursi).